JOURNAL OF GEOPHYSICAL RESEARCH, VOL. 116, D21201, doi:10.1029/2011JD016016, 2011

Optical characterization of continental and biomass-burning aerosols over Bozeman, Montana: A case study of the aerosol direct effect

Amin R. Nehrir,[1] Kevin S. Repasky,[1] John A. Reagan,[2] and John L. Carlsten[3]

Received 10 April 2011; revised 5 August 2011; accepted 18 August 2011; published 2 November 2011.

[1] Atmospheric aerosol optical properties were observed from 21 to 27 September 2009 over Bozeman, Montana, during a transitional period in which background polluted rural continental aerosols and well-aged biomass-burning aerosols were the dominant aerosol types of extremely fresh biomass-burning aerosols resulting from forest fires burning in the northwestern United States and Canada. Aerosol optical properties and relative humidity profiles were retrieved using an eye-safe micropulse water vapor differential absorption lidar (DIAL) (MP-DIAL), a single-channel backscatter lidar, a CIMEL solar radiometer as part of the Aerosol Robotic Network (AERONET), a ground-based integrating nephelometer, and aerosol products from Moderate Resolution Imaging Spectroradiometer (MODIS) Terra and Aqua. Aerosol optical depths (AODs) measured during the case study ranged between 0.03 and 0.17 (0.015 and 0.075) at 532 nm (830 nm) as episodic combinations of fresh and aged biomass-burning aerosols dominated the optical depth of the pristinely clean background air. Here, a pristinely clean background refers to very low AOD conditions, not that the aerosol scattering and absorption properties are necessarily representative of a clean aerosol type. Diurnal variability in the aerosol extinction to backscatter ratio (S_a) of the background atmosphere derived from the two lidars, which ranged between 55 and 95 sr (50 and 90 sr) at 532 nm (830 nm), showed good agreement with retrievals from AERONET sun and sky measurements over the same time period but were consistently higher than some aerosol models had predicted. S_a measured during the episodic smoke events ranged on average from 60 to 80 sr (50 to 70 sr) at 532 nm (830 nm) while the very fresh biomass-burning aerosols were shown to exhibit significantly lower S_a ranging between 20 and 40 sr. The shortwave direct radiative forcing that was due to the intrusion of biomass-burning aerosols was calculated to be on average -10 W/m^2 and was shown to compare favorably with regional-scale forcing calculations using MODIS-Terra and AERONET data in an effort to assess the accuracy of estimating the regional-scale aerosol direct radiative forcing effect using aerosol optical properties measured from a single rural site such as Bozeman, Montana.

Citation: Nehrir, A. R., K. S. Repasky, J. A. Reagan, and J. L. Carlsten (2011), Optical characterization of continental and biomass-burning aerosols over Bozeman, Montana: A case study of the aerosol direct effect, *J. Geophys. Res.*, *116*, D21201, doi:10.1029/2011JD016016.

1. Introduction

[2] Aerosols affect the Earth's radiation budget through direct scattering and/or absorption of the incoming shortwave solar radiation [*Shine and Forster*, 1999; *Haywood and Boucher*, 2000; *Yu et al.*, 2006; *Forster et al.*, 2007]. The aerosol direct effect, best described as the interaction of atmospheric aerosols with the incoming solar radiation, can be modeled as a change in the planetary albedo [*Coakley and Chylek*, 1975; *Charlson et al.*, 1991; *Charlson*, 1992; *Chylek and Wong*, 1995; *Haywood and Shine*, 1995; *Wendisch et al.*, 2001; *McComiskey et al.*, 2008]. Initial modeling of the change in the planetary albedo as a result of natural and anthropogenic atmospheric aerosols was developed [*Coakley and Chylek*, 1975; *Charlson et al.*, 1991; *Charlson*, 1992; *Chylek and Wong*, 1995; *Haywood and Shine*, 1995] and indicated that the globally averaged radiative forcing resulting from anthropogenic sulfates was approximately -1.1 W/m^2, resulting in a net cooling that is comparable, but opposite in sign, to the radiative forcing resulting from the anthropogenic increase in atmospheric carbon dioxide [*Charlson et al.*, 1991]. The initial modeling

---

[1] Department of Electrical and Computer Engineering, Montana State University, Bozeman, Montana, USA.

[2] Department of Electrical and Computer Engineering, University of Arizona, Tucson, Arizona, USA.

[3] Physics Department, Montana State University, Bozeman, Montana, USA.

0148-0227/11/2011JD016016

of the aerosol direct effect was refined to include absorbing aerosols with the realization that under the right conditions, the aerosol direct effect can lead to a positive radiative forcing [*Chylek and Wong*, 1995; *Haywood and Shine*, 1995; *Wendisch et al.*, 2001]. Further refinements to the aerosol direct effect modeling allow the importance of the angular dependence of the phase function to be accounted for by incorporating the solar zenith angle [*Wiscombe and Grams*, 1976; *Chylek and Wong*, 1995; *Nemesure et al.*, 1995; *Wendisch et al.*, 2001].

[3] While improvements in the understanding of the radiative forcing resulting from anthropogenic aerosols has increased, the Intergovernmental Panel on Climate Change (IPCC) report issued in 2007 indicates the globally averaged top of the atmosphere (TOA) radiative forcing that is due to the aerosol direct effect associated with anthropogenic aerosols ranges between −0.5 and ±0.4 W/m^2 [*Forster et al.*, 2007]. This large range reflects the difficulty inherent in understanding the radiative effects of atmospheric aerosols that are due to the spatial, temporal, and compositional variabilities of atmospheric aerosols.

[4] The TOA radiative forcing that is due to aerosols depends on their optical properties, including the aerosol optical depth (AOD), the single-scatter albedo (SSA), the size distribution, the complex index of refraction, as well as the albedo of the underlying scene [*Haywood and Boucher*, 2000; *Wendisch et al.*, 2001; *Yu et al.*, 2006; *McComiskey et al.*, 2008]. Active and passive optical remote sensing instruments provide a means of measuring the aerosol optical properties needed for estimating the radiative forcing associated with aerosols [*Russell et al.*, 1979, 1997; *Loeb and Manalo-Smith*, 2005; *Ferrare et al.*, 2006; *Yu et al.*, 2006; *Pahlow et al.*, 2006; *Ricchiazzi et al.*, 2006; *Hallar et al.*, 2006; *Johnson et al.*, 2009; *Moffet and Prather*, 2009]. During this case study, a single-channel elastic backscatter lidar operating at 532 nm [*Repasky et al.*, 2011], an eye-safe micropulse water vapor differential absorption lidar (DIAL) (MP-DIAL) operating at 830 nm [*Nehrir et al.*, 2009, 2011], a sun-sky scanning solar radiometer [*Holben et al.*, 2001], and a ground-based integrating nephelometer were used to study the aerosol optical properties during a rapid buildup of forest fire smoke over Bozeman, Montana, between 21 and 27 September 2009. Data from the Moderate Resolution Imaging Spectroradiometer (MODIS) (https://modis.gsfc.nasa.gov) aboard the Terra satellite was used to provide additional information regarding the mean surface reflectance and AOD that was needed for radiative forcing estimates resulting from the rapid buildup of the forest fire smoke over Bozeman, Montana. MODIS and Aerosol Robotic Network (AERONET) data were then used to estimate the radiative forcing over the northwestern United States, and the results from the regional calculations based on the satellite and AERONET data were compared to radiative forcing calculations conducted using the suite of instruments at Bozeman, Montana, primarily the AOD measurements from AERONET in place of MODIS-derived AODs.

2. Instrumentation, Inversions, and Geography

2.1. Site Location and Geography

[5] The data presented in this case study were collected at the Bozeman, Montana (45.679°N, 111.037°W, elevation 1530 m) AERONET/micropulse lidar (MPL) site in the northern Rocky mountain range. This site has been part of the AERONET and MPLNET programs since 2006 and 2010, respectively, and provides a natural setting for observing and studying the variabilities in both annual and episodic aerosol and atmospheric gas trends in an uncontaminated background environment. Bozeman, Montana, sits at the eastern edge of the Gallatin Valley with the Bridger Mountain Range to the northeast, the Gallatin and Spanish Peak Mountain Ranges to the south and southwest, the Tobacco Root Mountains to the west, and the Horseshoe Hills to the northwest. The complex surrounding terrain yields unique diurnal mesoscale meteorology with daytime upslope (westerly) winds and nighttime downslope (easterly) winds. The unique geographic location of the remote sensing facility coupled with the general westerly flows dominant over the Northwest allows for monitoring of a wide range of aerosol types over the exceptionally clean background aerosol levels. Dominant aerosol types observed at the Bozeman, Montana, site include relatively unaged biomass-burning aerosols from nearby forest fires, aged long-range-transported smoke from the West Coast of the United States and Canada, polluted continental aerosols, dust from agricultural activities, and southeast Asian dust.

2.2. Instrumentation and Methods

2.2.1. Micropulse Water Vapor DIAL (MP-DIAL)

[6] The MP-DIAL is a diode-laser-based micropulse eye-safe instrument operating near 830 nm [*Nehrir et al.*, 2009; *Nehrir et al.*, 2011] and was operated almost continuously throughout the duration of this case study, from 21 to 27 September 2009. A tunable external cavity diode laser is used to injection seed two cascaded tapered semiconductor optical amplifiers (TSOAs), producing up to 2 μJ of peak energy over 1 μs pulse durations. A duty cycle of 2% for this case study yielded a maximum resolvable range of 7.5 km with a spatial resolution of 150 m, which was oversampled by a 20 MHz digital data logger, resulting in 7.5 m vertical range resolution with 150 m ambiguity in the return range. The receiver utilizes a 28 cm Schmidt-Cassegrain telescope and an avalanche photodiode detector operating in a Geiger mode. The receiver has a 170 μrad full-angle field of view. Water vapor number density and aerosol extinction profiles were averaged over 30 min and 4 min, respectively, to yield a reasonable signal-to-noise ratio. Humidity fields were derived using number densities retrieved from the MP-DIAL as well as from colocated temperature and pressure profiles obtained from daily VAISALA RS92 radiosonde measurements. A detailed description of the MP-DIAL instrument and water vapor retrievals are presented by *Nehrir et al.* [2011].

[7] Aerosol extinction profiles were retrieved using the off-line channel of the MP-DIAL. For the 830 nm elastic backscatter channel, the lidar equation for the aerosol backscatter component of the retrieved signal was inverted using the assumption of a constant extinction to backscatter ratio ($S_{a,830}$) with respect to altitude. The AOD at 830 nm, calculated from the wavelength-dependent extinction Ångström coefficient from the two nearest channels (675 nm, 870 nm) of the solar radiometer, was used as a constraint on the lidar inversion [*Eck et al.*, 1999]. An iterative solution to the Fernald lidar inversion [*Fernald et al.*, 1972; *Fernald*, 1984] was completed by varying the $S_{a,830}$ until the AOD from the

MP-DIAL was in good agreement with the AOD from the solar radiometer. A standard atmosphere was modeled [*Kovalev and Eichinger*, 2004] such that the Rayleigh backscatter coefficient was used to retrieve the instrument calibration constant between 5.5 and 6.0 km, where the Rayleigh scattering dominates the return signal. In the presence of cirrus clouds, the MP-DIAL is calibrated below the cirrus deck. It should be noted that the assumption of a constant $S_{a,830}$ with altitude introduces possible errors in the retrieved extinction and backscatter profiles. As far as the typical impact of S_a variability, numerous observations with an airborne high spectral resolution lidar (HSRL) [*Reagan et al.*, 2007; *McPherson et al.*, 2010; *Burton et al.*, 2010] have shown that S_a and extinction profile and AOD retrievals made with the assumption of S_a being constant for the region observed (e.g., the boundary layer) typically yield an S_a close to the mean S_a for the region (with observed variability typically fairly random and within ~20% of the mean) and AODs that are fairly accurate (i.e., accurate within ~15%–20%). Another potential source of error in the aerosol retrievals arises from the incomplete overlap function of the MP-DIAL from near surface up to 0.75 km. The extinction profiles retrieved from the lidar are extended to the surface by a linear interpolation between the aerosol extinction measured at initial overlap from the lidar to the aerosol extinction measured at the surface using an integrating nephelometer operating at 530 nm. The aerosol extinction at the ground at 830 nm is once again calculated using the Ångström coefficient retrieved from the two nearest channels (500 and 870 nm) of the solar radiometer.

2.2.2. Elastic Backscatter Lidar

[8] Aerosol extinction profiles were also collected throughout the duration of this case study using a non-eye-safe single-channel elastic backscatter lidar [*Repasky et al.*, 2011]. The lidar utilizes the frequency-doubled output from a flashlamp-pumped Q-switched neodymium: yttrium/aluminum/garnet (Nd:YAG) laser for the laser transmitter. The laser output has 100 mJ pulses with a pulse duration of 9.9 ns and a pulse repetition frequency of 20 Hz. A 28 cm diameter Schmidt-Cassegrain telescope and a gated photomultiplier tube (PMT) yield a full-angle field of view of 2 mrad, allowing for aerosol extinction retrievals up to 20 km with 0.75 m vertical range resolution set by a 14 bit 200 MHz two-channel analog to digital (A/D) data logger. Aerosol extinction profiles were temporally and spatially averaged over 2 min and 15 m, respectively, to yield reasonable signal-to-noise ratios because of the low-background aerosol loading. Aerosol extinction profiles using the single-channel lidar were retrieved from the backscattered signal at 532 nm in a manner similar to that described for the MP-DIAL.

2.2.3. Ground-Based Integrating Nephelometer

[9] The scattering component of the aerosol extinction at the surface was measured with an M-903 Integrating Nephelometer (Radiance Research, Seattle) operating at 530 nm. The nephelometer was operated at a temperature slightly above ambient. This, along with the fact that the humidity was always considerably below saturation as measured by nearby weather stations as well as by the MP-DIAL, resulted in the measurement of dry aerosols. Airflow through the instrument was set at 5 liters per minute (Lpm). Data were averaged and logged over 15 min, and calibration was executed by filling the scattering volume with CF-22 before and after the experiment. The instrumental zero point was checked every few days by inserting an absolute filter. According to the drifts in the zero point and in the calibration, we infer that the measured scattering component of the aerosol extinction at 530 nm is precise to $\pm 1\ \mathrm{Mm}^{-1}$. A major source of error in nephelometry arises from truncation errors at 0° and 180°. The error tends to cancel out for measurements of light scattering by submicron particles, in part because they scatter only a slightly larger fraction of the total scattering into the forward and backward directions than do the calibration gases. As particles become larger, a larger fraction of their scattered light is in the forward and backward directions, and the truncation error increases. For coarse particles having diameters between 2.5 and 10 μm, light scattering measured by nephelometers are approximately half of the total light scattering [*Moosmüller and Arnott*, 2003]. Although potentially large, the angular truncation errors are not considered in this study as the nephelometer data are primarily used for qualitative analysis of the temporal variability of aerosols at the observation site.

2.2.4. CIMEL Solar Radiometer

[10] A CIMEL CE-318 sun-sky solar radiometer has been operating at Montana State University as part of the NASA AERONET global network [*Holben et al.*, 1998, 2001] since 2006. Nine solar irradiance measurements were made every 15 min during clear sky conditions at 340, 380, 440, 500, 675, 870, 940, 1020, and 1240 nm. The AOD was then calculated using all of the extinction measurements except the 940 nm channel according to methods presented by *Holben et al.* [1998, 2001]. The AODs at 532 and 830 nm used as the constraints for the lidar inversions were calculated by using the wavelength dependence of the measurements at the nearest two channels. The extinction Ångström coefficient α that represents the wavelength dependence of the aerosol extinction coefficients was calculated using $\tau = \tau_0(\lambda/\lambda_0)^{-\alpha}$, where τ is the AOD and λ is the wavelength. The Ångström coefficient retrieved from AERONET AOD measurements provides information regarding the column average size of the dominating aerosol type, where larger values imply a relatively higher ratio of small particles and smaller values for higher ratios of larger particles. Other aerosol properties such as the aerosol size distribution, scattering phase function ($P(\theta)$), single-scatter albedo (ω), and complex refractive indices used for the lidar inversions and radiative forcing calculations were retrieved using the CIMEL sky radiance measurements obtained in an almucantar geometry using the 440, 675, 870, and 1020 nm channels. The CIMEL-derived lidar ratio ($S_a = 4\pi/(\omega P(180°))$), which is retrieved using the diffuse sky radiance measurements at the aforementioned wavelengths and constrained in an inversion using the direct sun measurements, is used as a pseudo-independent or alternative cross check to the lidar retrieved S_a that uses only the direct sun measurement as a constraint on the Fernald lidar inversion [*Dubovik and King*, 2000; *Dubovik et al.*, 2000]. The uncertainty in the CIMEL retrievals of ω is estimated to be ~0.03–0.07 while the uncertainty in $P(\theta)$ is not well known, although both become greater at lower AODs and are discussed in detail by *Dubovik and King* [2000] and *Dubovik et al.* [2000]. The expected

accuracy for the volume size distribution for particles with $r \geq 0.5$ μm is 15%–25% while for particles with $r < 0.5$ μm it is expected to range between 25% and 100%.

3. Aerosol Optical and Microphysical Characterization

3.1. Satellite Observations of Regional Aerosol Optical Depths

[11] The aerosol optical properties obtained from a combination of active and passive remote sensors from ground- and satellite-based platforms can be used to estimate the regional aerosol radiative forcing. To evaluate the spatial variability of the various types of aerosols measured throughout this case study, aerosol data products were used from the MODIS instrument on board the Terra and Aqua satellites. Figure 1 shows the MODIS-Aqua true color and hot spot fire activity in the near vicinity of Bozeman, Montana, the AOD from MODIS-Terra, and the 5 day NOAA Hybrid Single-Particle Lagrangian Integrated Trajectory (HYSPLIT) back trajectory analysis in the first, second, third, and fourth rows for 24, 25, 26, and 27 September 2009, respectively. These four days correspond to periods of rapid transition from a relatively clean aerosol background level dominated by a combination of aged biomass-burning aerosols and polluted continental aerosols to an atmosphere dominated by aged and relatively fresh biomass-burning aerosols in succession.

[12] The daily MODIS-Terra AOD (MOD04) at 550 nm and MODIS-Aqua visible hot spot images show the development and progression of biomass-burning aerosols over the northwest region of the country. The true color and hot spot images show light fire activity in the northwestern region of Montana on 24 September, as indicated by the red dots, but also shows little presence of biomass-burning aerosols over Bozeman, as indicated by the blue target. MODIS-Terra measurements for the same day show seasonably low AODs of less than 0.05 near Bozeman, but also show the presence of a large aerosol plume extending from northwestern California into northwestern Montana and Canada. The HYSPLIT back trajectory analysis and knowledge of fire activity in the northwest region between 24 and 25 September 2009 confirms the broad aerosol source to be biomass burning. On 25 September 2009, the aerosol plume was pushed down into central Montana, resulting in relatively high AODs, ranging between 0.1 and 0.35 and dominated by 3–4 day aged biomass-burning aerosols. The short-lived plume was then pushed out on 26 September, with a northwesterly front causing a brief void of an aerosol-loaded atmosphere over Bozeman before a plume of fresh smoke resulting from advected biomass-burning aerosols from forest fires in western Montana intruded directly over Bozeman. This event is clearly depicted from the MODIS-Terra AOD and MODIS-Aqua true color images from 26 September 2009. The temporal difference between the MODIS-Terra AOD measurements (18:20 UTC) and the MODIS-Aqua true color images (composite between 20:05, 20:10, and 21:45 UTC) shows the flushing out of the broad aged aerosol plume and the subsequent intrusion of the fresh smoke directly over Bozeman. The HYSPLIT back trajectory analysis between 25, 26, and 27 September 2009 also indicates the shift in the wind direction from northwest to west, advecting fresh biomass-burning aerosols from western Montana directly over the observation site. MODIS-Aqua AOD measurements from 27 September 2009 indicate the presence of a highly directional aerosol plume from west central Montana over Bozeman. MODIS rapid response hot spot imagery and the HYSPLIT back trajectory analysis indicate the source and origin of the relatively unaged aerosols to be biomass-burning resulting from forest fire smoke in the Bitterroot Mountain Range in west central Montana.

3.2. Ground-Based Observations of Aerosol Optical Properties Over Bozeman, Montana

[13] The aerosol optical properties of the varying aerosol types throughout this case study were also studied using a suite of ground-based instruments, including a water vapor MP-DIAL, a single-channel backscatter lidar, a CIMEL solar radiometer, and an integrating nephelometer. The eye-safe water vapor MP-DIAL operating at 830 nm provided near-full-time autonomous data during the seven day study while the non-eye-safe backscatter lidar operating at 532 nm had Federal Aviation Administration (FAA) permission to operate only from 2:30 P.M. to 1:00 A.M. local time (UTC–6). A plot of the comparison of the AOD measured by the solar radiometer and the two lidars as a function of time is shown in Figure 2. The AOD constraint for the nighttime inversion was achieved by assuming a linearly changing AOD between the last CIMEL AOD measurement made during the evening and the first AOD measurement made the following morning. This assumption allowed a qualitative understanding of the changing aerosol extinction profiles during the nighttime but did not affect the radiative forcing calculations resulting from the aerosol direct effect presented in section 4, as daytime data were used for the calculations. A clear transition can be seen from a clean atmosphere, with average AODs ranging from 0.02 to 0.05 at 830 and 532 nm, respectively, to higher AODs approaching 0.15 at 532 nm as the biomass-burning aerosols were transported into the Gallatin Valley. Patchy cirrus cloud contamination of the lidar and solar radiometer AOD measurements is evident at the beginning and end of the case study and limited the accuracy of the aerosol optical properties at these times. The agreement otherwise between the AOD measured using the solar radiometer and the AOD resulting from the completed lidar inversions at the 532 and 830 nm wavelengths is expected since the AOD measured using the solar radiometer is used to constrain the lidar inversions. The relatively good agreement achieved between the lidar S_a retrievals and the CIMEL-derived S_a, to be discussed next, provides a stronger indication that various systematic influences such as the assumption of constant S_a with height as well as the Rayleigh normalization have not significantly impacted the lidar retrievals.

[14] The iterative lidar retrievals based on the Fernald inversion technique described in section 2 provide the S_a of the dominant aerosols that can then be used to classify different aerosol types [*Cattrall et al.*, 2005; *Omar et al.*, 2005]. Figure 3a (Figure 3b) are plots of the S_a and the corresponding error (in red) for the 532 nm (830 nm) wavelength over the seven day period retrieved from both the solar radiometer (green boxes) and lidars (black solid line). The errors in the lidar retrievals of S_a represent the standard deviations in the inversion arising from the uncertainties in the constraining AODs. The total uncertainty in the AOD measurements for a

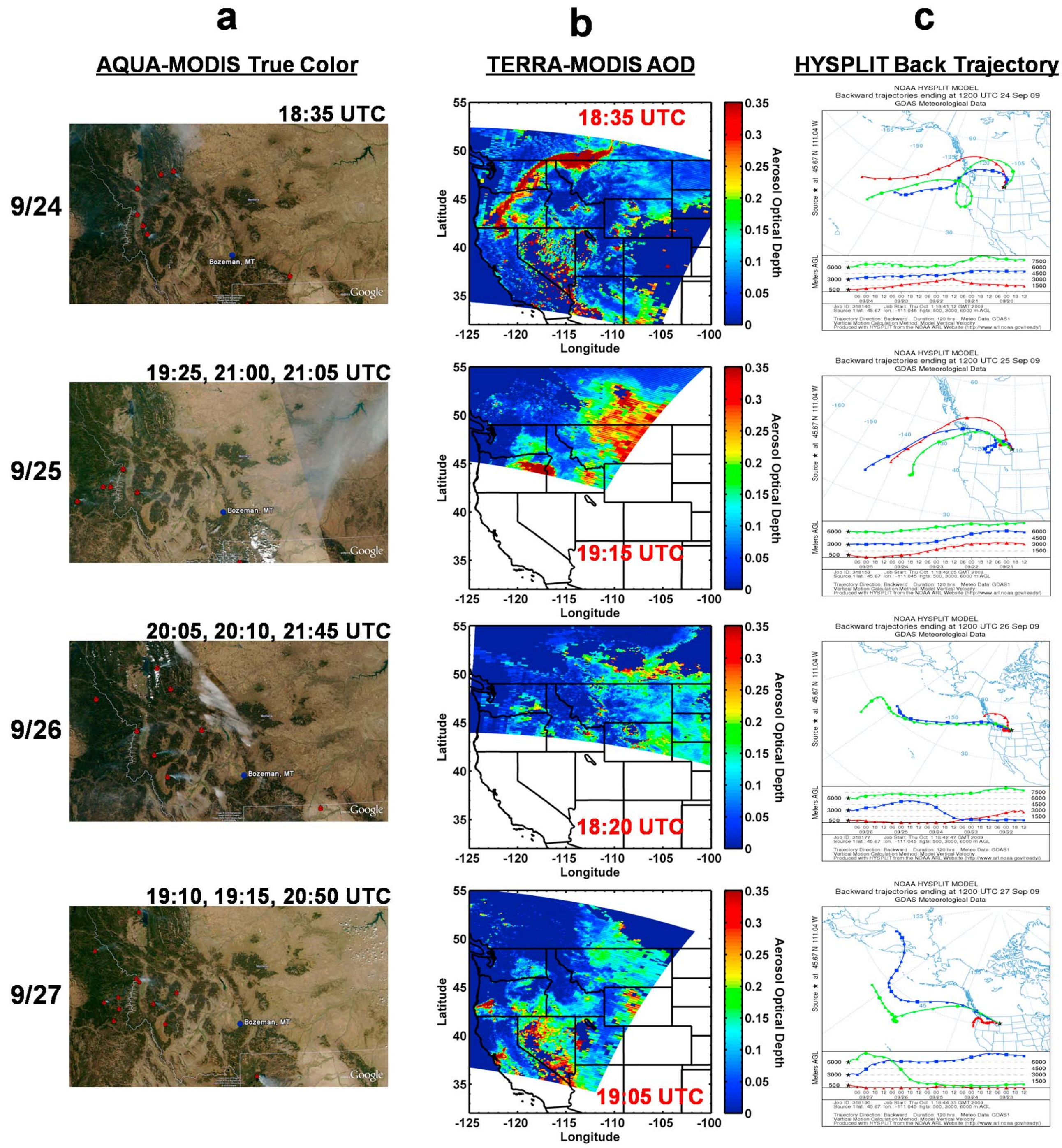

Figure 1. (a) Aqua-MODIS rapid response fire counts surrounding Bozeman, Montana, from 24 to 27 September 2009; (b) Terra-MODIS MOD04 AOD over the northwestern United States and Canada during the same time period; (c) NOAA HYSPLIT 5 day back trajectory analysis.

newly calibrated CIMEL Sun photometer given cloud-free conditions is of the order of ±0.01for visible wavelengths greater than 440 nm [*Smirnov et al.*, 2000]. The estimates of the CIMEL-derived S_a uncertainties is dependent on the cumulative error resulting from ω and $P(180)$ and is expected to fall in the range of 15%–25%, with larger uncertainties at lower AODs [*Dubovik et al.*, 2000]. Reasonable agreement between the solar radiometer and the lidars retrievals can be seen throughout the duration of the case study. Diurnal variability in the S_a at both wavelengths was clearly evident from both the lidar and solar radiometer measurements in the first three days of the study and was primarily attributed to the local mountain-plains wind systems. The tracking of the diurnal trends of the S_a, given low-background AODs in both the CIMEL and the lidar measurements, suggests the validity of the lidar retrievals. Westerly upslope daytime winds at lower elevations blowing from the valley toward the mountains resulted in the transport of anthropogenic

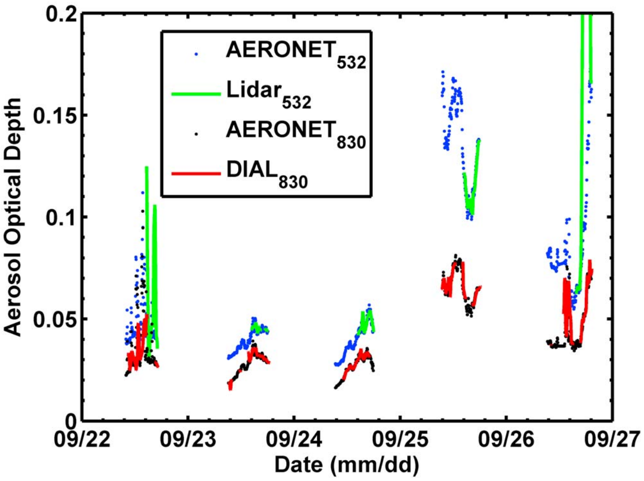

Figure 2. Aerosol optical depth observations from AERONET (532 nm (830 nm) AOD estimated from the 500–675 nm (675–870 m) channels using the Ångström coefficient), single-channel elastic lidar-integrated extinction resulting from AEROENT AOD constrained Fernald inversion, and 830 nm DIAL integrated extinction also resulting from AERONET AOD constrained Fernald inversion.

aerosols such as polluted continental aerosols from nearby urban areas, resulting in lower S_a ranging on average from 60 to 80 sr (50 to 70 sr) at 532 nm (830 nm), which are generally consistent with the AERONET clustering models [*Cattrall et al.*, 2005; *Omar et al.*, 2005]. Clear skies formed a stable nocturnal boundary layer and brought nighttime downslope winds blowing east from the mountains to the valley floor, transporting relatively clean background aerosols with a weak accumulation mode that was observed to have significantly higher peak values of S_a of approximately 55–95 sr (50–90 sr) at 532 nm (830 nm) by the morning. During the second half of the case study, the average daily S_a measured by both lidars as well as by the solar radiometer were noticeably lower because of the influx of biomass-burning aerosols over Bozeman, Montana. Average S_a ranged between 35 and 60 sr (20 and 45 sr) at 532 nm (830 nm), which show moderate agreement with the S_a derived from AERONET cluster analysis for biomass-burning aerosols. A further discussion regarding the comparison of this case study with aerosol clustering models developed by *Cattrall et al.* [2005] and *Omar et al.* [2005] is presented in section 4. These active- and passive-derived aerosol inversions have also been successfully demonstrated in a previous case study [*Repasky et al.*, 2011] in which lidar and AERONET Sun photometer measurements of S_a showed good agreement during a biomass-burning aerosol intrusion event over Bozeman, Montana.

[15] Aerosol extensive properties were also measured using the two lidars to monitor the temporal-spatial distributions of aerosols over Bozeman, Montana. Time-height cross sections of the aerosol extinctions at 532 and 830 nm as a result of the *Fernald* [1984] lidar inversion are shown in Figures 4a and 4b, respectively. A relatively clean (i.e., low-AOD) atmosphere was present in the first half of the case study, as indicated by the low aerosol extinctions in the boundary layer as well as from the low AODs shown in Figure 2. Average boundary layer extinction coefficients between 21 and 24 September 2009 were approximately 18 and 12 Mm^{-1} at 532 and 830 nm, respectively, with an average boundary layer height of approximately 1.5 km. High-altitude cirrus clouds early in the case study contaminated the return signals from the high pulse repetition rate MP-DIAL, but allowed for continuous qualitative measurements of the aerosol extinction profiles. The biomass-burning aerosols can be seen pushing into the Gallatin Valley starting late on 24 September 2009. Flushing out of the aged smoke transported from the northwest region of the country from 25 and 26 September, as shown in Figure 1, can be seen on the evening of 26 September 2009. Fresh smoke transported from nearby fires in western Montana shown in Figure 1 is indicated by high extinction coefficients during 26 and 27 September. The average boundary layer aerosol extinction coefficients between 24 and 27 September were approximately 50 and 35 Mm^{-1} at 532 and 830 nm, respectively, with an average boundary layer height of approximately 2.5 km, a noticeable increase over the back-

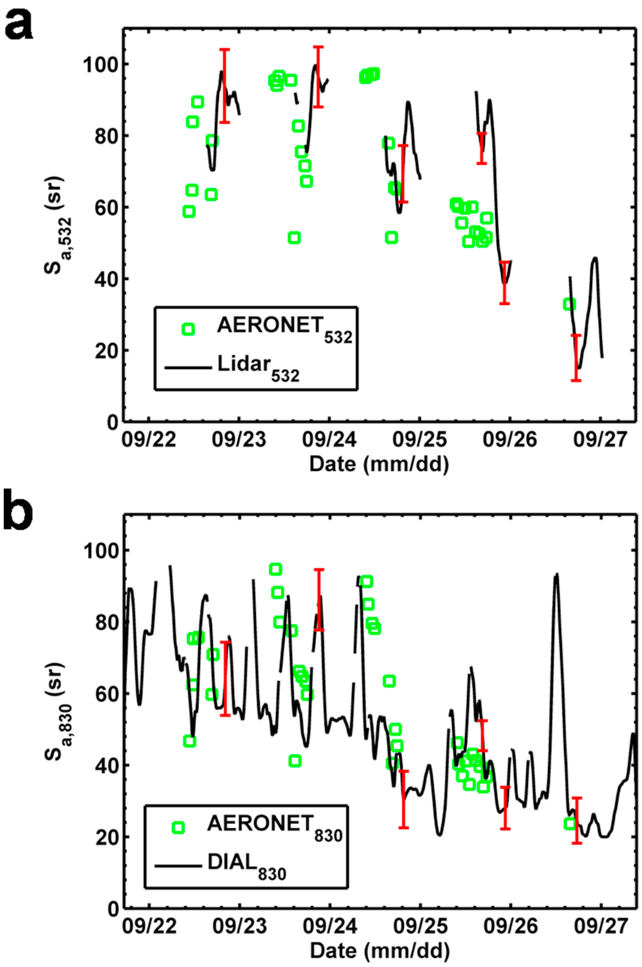

Figure 3. (a) Summary of 532 nm S_a retrievals from AERONET (estimated from the 500 nm channel) almucantar scan inversions, and elastic lidar inversions resulting from the constrained iterative Fernald retrievals. (b) Summary of 830 nm S_a retrievals from AERONET (estimated from the 870 nm channel), and DIAL retrievals resulting from the constrained iterative Fernald inversions.

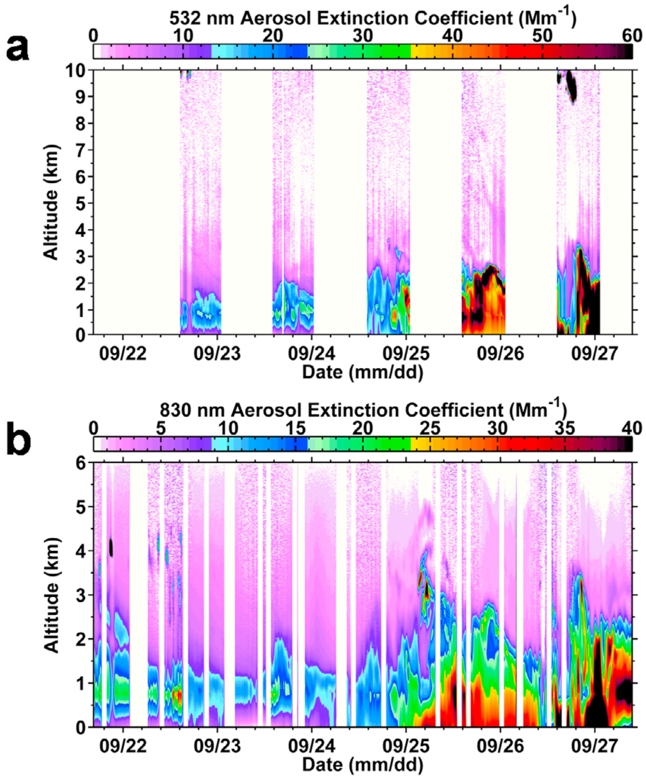

Figure 4. (a) Lidar-measured 532 nm aerosol extinction coefficient from 21 to 27 September 2009, over Bozeman, Montana. (b) MP-DIAL-measured 830 nm aerosol extinction coefficient from 21 to 27 September 2009, over Bozeman, Montana.

ground levels. The aerosol extinction profiles plotted in Figure 4 resulted from both scattering and absorption of the varying aerosol types during this case study. The AERONET level 1.5 SSA aerosol product was used as a measure of the ratio of the aerosol scattering extinction to the total aerosol extinction, which is important for understanding the direct shortwave radiative forcing resulting from the aerosol direct effect. A plot of the daily averaged SSA as a function of time resulting from the solar radiometer retrieval is shown in Figure 5 for both the 532 and 830 nm wavelengths. The error bars represent the standard deviations over the daily measurements, and the individual SSA retrievals are estimated to have ~0.03–0.07 uncertainty [*Dubovik et al.*, 2000]. The SSAs at the two wavelengths are calculated using a polynomial fit from the SSAs at the two nearest radiometer channels. The decreasing SSA between 21 and 24 September 2009 indicated the presence of more absorptive aerosols, assumed to be primarily from well-aged biomass-burning aerosols as well as from local anthropogenic sources from within the valley. The SSA increase from 24 to 27 September was attributed to the inflow of relatively fresh biomass-burning aerosols from forest fires in western Montana. The good correlation between the increase in the SSA and the decrease in the S_a from Figure 3 suggests that the aging of the aerosols throughout the transport process decreases the aerosol absorption, most likely resulting from a deposition process (particle aggregation) of the fine-mode aerosols and gravitational sedimentation of the coarse-mode aerosols [*Amiridis et al.*, 2009].

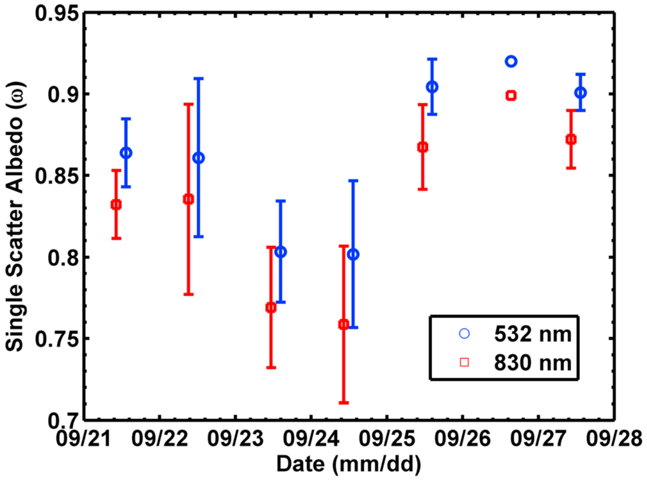

Figure 5. AERONET measurements of single-scatter albedo (ω) at 532 and 830 nm throughout the duration of the case study over Bozeman, Montana.

[16] The total scattering by atmospheric aerosols is described by the phase function, which is dependent on the complex index of refraction, the depolarization ratio, and the size distribution of the aerosols. The average phase function for each day of the observational period is shown in Figure 6 for the 532 nm wavelength and was calculated using a polynomial fit from the two AERONET-retrieved phase functions from the two nearest channels. The phase functions show the same trends (i.e., lower backscatter for higher S_a) as in the S_a plots in Figure 3, and as the phase functions show scattering effects, the changes in S_a in Figure 3 are driven in part by scattering effects (e.g., size distribution and refractive index changes). The larger values of the phase function for the backscatter direction during 25–27 September 2009 indicated that the scattering particles were smaller on average

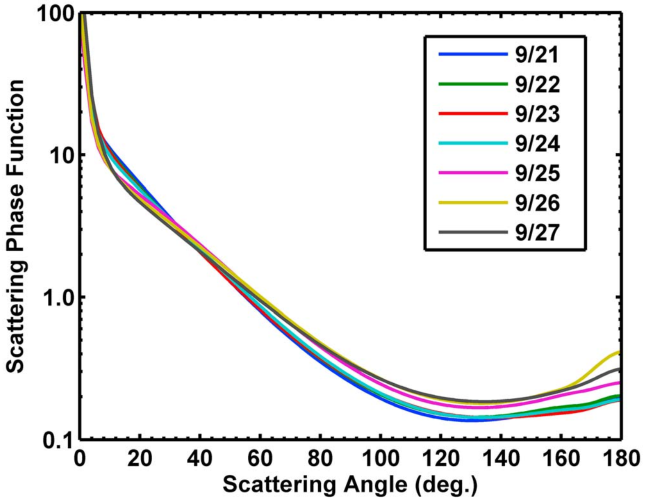

Figure 6. Measurements of the scattering phase function resulting from the AERONET almucantar scan inversions from 21 to 27 September 2009 over Bozeman, Montana.

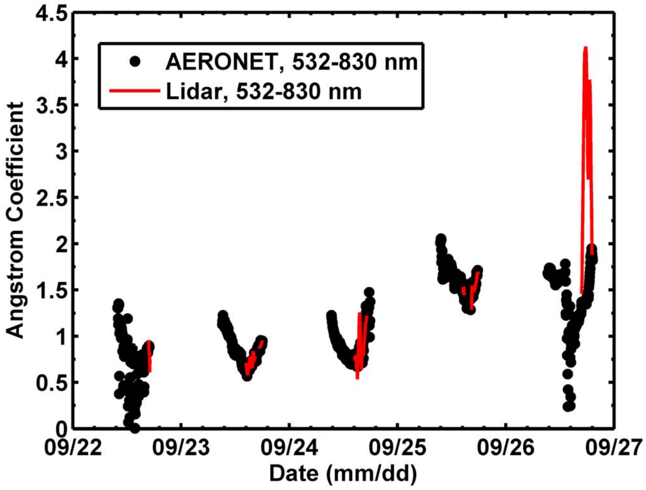

Figure 7. CIMEL measurements of the Ångström coefficient (532–830 nm) compared against the lidar-derived Ångström coefficient (532 nm lidar–830 nm DIAL) throughout the duration of the case study.

during these days than during 21–24 September 2009. From Mie scattering theory, this is consistent with an increase in smaller aerosols associated with the intrusion of biomass-burning aerosols, as expected based on the back trajectory analysis seen in Figure 1 coupled with the increased aerosol loading seen in Figure 4 during the latter half of the case study. The atmospheric aerosol extinction profiles measured with the two lidars depend on the complex index of refraction, the particle size distribution, and the scattering phase function. The Ångström coefficient calculated using the wavelength dependence of the extinction profiles from the lidar returns is sensitive to changes in these parameters and is plotted as a function of time in Figure 7. The 532 and 830 nm lidar extinction retrievals (Figure 4) were used to calculate the Ångström coefficient (red line). The CIMEL-derived Ångström coefficients (black dots) were calculated from the Sun photometer AOD measurements at 532 and 830 nm, which were calculated using the methods described earlier. The higher Ångström coefficient, ranging up to approximately two on 25–27 September 2009, is consistent with aerosols associated with biomass burning [*Eck et al.*, 1999]. That is, the AOD spectral dependence that is due to more large than small particles drives the Ångström coefficient lower (toward zero), while the opposite (more small than large particles) drives the Ångström coefficient higher (toward ~2). The anomalous upswing in the Ångström coefficient measured using the lidar at the end of the case study resulted from transient or patchy cirrus cloud contamination of the lidar returns.

[17] It is also worth noting that while the CIMEL inversions for SSA may become less reliable at such low optical depths [*Dubovik et al.*, 2000], such as the case during the beginning part of this observational period, the AODs themselves and the Ångström coefficients are more reliable. The average Ångström coefficient (532–830 nm) measured from CIMEL during the first half of the case study was approximately 0.8, resulting from what is thought to be a combination of polluted continental aerosols as well as long-aged smoke residual aerosols that may with time lose the strength of its accumulation mode because of the growth of the particles into the coarse mode. An average Ångström coefficient (532–830 nm) ranging between 1.2 and 1.4 was measured for low-AOD days during the summer of 2009, which is significantly higher than the background period during this case study and is an indication that inversions resulting from the direct radiance measurements did not greatly suffer from systematic and or random errors resulting from the very low AODs.

[18] As a general assessment on the validity of AERONET inversions for AODs approaching 0.05, theoretical scattering computations to determine an independent S_a for a given AERONET volume size distribution to be discussed later and various values of the complex index of refraction were conducted to evaluate the consistency of the AERONET S_a inversions. Figure 8, a scatterplot of the S_a at 532 nm retrieved from AERONET, compares the results with the Mie scattering calculations, and they show satisfactory agreement with one another. Larger discrepancies are noticeable between the AERONET retrievals and the Mie scattering calculations early in the week when low AODs were measured, but the general agreement provides greater confidence in the AERONET retrievals. As a further check into the validity of the Mie scattering model as well as the accuracy of the AERONET retrievals throughout the duration of this case study, Mie scattering computations for 23 and 27 September 2009 (low and high AODs, respectively) were further analyzed. Figure 9a shows the two volume size distributions and the corresponding standard deviations (only on 23 September) over all size distribution measurements from those particular days that were used as inputs for the Mie scattering calculations shown in Figure 9b. For 23 September 2009, an average volume size distribution from that day was used as the input to the scattering calculations. Because the extremely fresh smoke was sampled only by AERONET on the morning of 27 September 2009 before it was flushed out of the valley, only one volume size distribution measured early in the morning was used for that day. Figure 9b shows the results of the of the Mie scattering computations for the

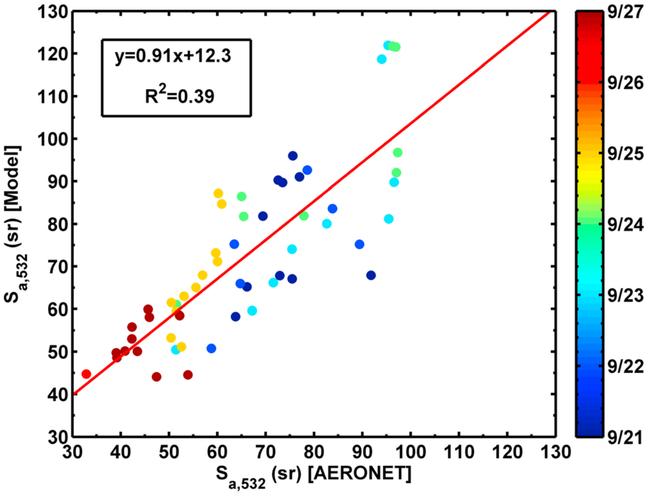

Figure 8. Scatterplot of AERONET retrievals of S_a at 532 nm compared against results from Mie scattering computations at 532 nm from 21 to 27 September 2009 over Bozeman, Montana.

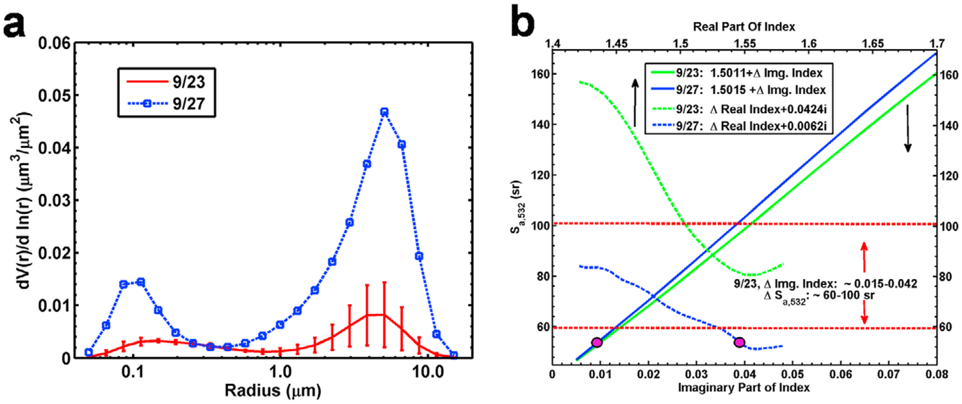

Figure 9. (a) AERONET retrieval of aerosol volume size distributions during periods in which low-background AODs (23 September 2009) and high AODs dominated by biomass-burning aerosols (27 September 2009) were present. (b) Results from Mie scattering computations for the two aerosol volume size distributions shown in Figure 9a.

two volume size distributions shown in Figure 9a. For the 23 and 27 September 2009 results shown, a daily average and a single value obtained from the first AERONET measurement of the complex index of refraction were used as inputs to the model, respectively. For each day, the real components of the indices were held constant and the imaginary components were varied (solid lines) and vice versa (dashed lines) to assess the sensitivity of the S_a for given changes in the complex index and size distribution. It is clear from Figure 9b that while the real part of the index plays a role in the daily variability in the S_a, the largest contributor to changes in the S_a is the complex component of the index. The purple circles signify the value of S_a (~55 sr) retrieved from AERONET on 27 September and the corresponding complex index resulting from the scattering model ($1.548 + 0.0085i$) which is in reasonable agreement with the AERONET retrieval of the complex index ($1.5015 + 0.0062i$) for that same time period. The red dashed lines indicate the range of calculated S_a associated with the range of the retrieved complex component of the index of refraction over all AERONET measurements on 23 September 2009.

[19] The spread in calculated S_a (~60–100 sr) corresponding to the spread in the AERONET-retrieved complex indices (~0.015–0.042) throughout the duration of the day shows very good agreement with the diurnal variability in the lidar-derived S_a (55–95 sr) on 23 September. Similar agreement trends with AERONET inversions were also observed for other low-AOD background days throughout the duration of this case study. The concurrence of these two partially independent retrieval methods speaks to the accuracy of the AERONET inversions during the extremely low background AODs, which were dominated by a combination of a well-aged smoke and polluted continental aerosols as well as during the episodic smoke events dominated in succession by aged and extremely fresh biomass-burning aerosols.

4. Comparison of Ground-Based Retrievals With Aerosol Models: AERONET and Lidar Compared and Combined

[20] A major difficulty in understanding the role of aerosols in the direct shortwave radiative forcing of the climate system results from the variability of aerosol types and the inability to continuously monitor their optical and microphysical properties in remote and rural sites worldwide [*Schulz et al.*, 2006]. The development of clustering models based on aerosol optical properties to classify different aerosol types has the potential to lower the uncertainty associated with the understanding of the direct shortwave radiative forcing and can help improve the role of aerosols in climate models [*Reagan et al.*, 2004, 2006, 2007; *Omar et al.*, 2005, 2009; *Cattrall et al.*, 2005]. Aerosol models for constraining lidar inversions at 532 and 1064 nm have been developed by *Cattrall et al.* [2005] and *Omar et al.* [2005] based on clustering analyses of AERONET radiance retrieval data. Both sets of aerosol models include core groupings of aerosol types based on the aerosol optical properties, which include urban-industrial or pollution, dust, smoke or biomass burning, and marine and oceanic sources. The optical properties of the aerosol models developed by Cattrall et al. and Omar et al. are summarized in Tables 1 and 2, respectively.

[21] A scatterplot of the S_a at 1020 nm as functions of the S_a at 532 nm based on the AERONET radiance retrievals are plotted in Figure 10 for the seven days during the observational period. The solid black line (red dashed line) indicates the range of S_a for the *Cattrall et al.* [2005] biomass-burning model (*Omar et al.* [2005] smoke model). The high S_a and relatively low Ångström coefficient between 21 and 24 September 2009 at 21:00 UTC suggests that the aerosols were relatively large in size and more absorptive than the aerosols measured during the latter part of the case study. The high S_a at both wavelengths measured from 21 to 24 September 2009 tend to be larger than the S_a associated with the different aerosol models developed by *Cattrall et al.* [2005] and *Omar et al.* [2005]. The S_a retrieved during this time period most closely fit the urban-industrial [*Cattrall et al.*, 2005] or the polluted continental aerosol models [*Omar et al.*, 2005]. The large discrepancy between the high S_a retrieved from the lidars and the two models is still under investigation, but is thought to be primarily due to the weak presence of extremely aged smoke with absorptive optical properties, as depicted in Figures 5 and 9b. The S_a measured after 21:00 UTC on 24–25 September

Table 1. Aerosol Model Parameters Derived by *Omar et al.* [2005, 2009]

Optical Physical Property	Dust	Smoke	Clean Continental	Polluted Continental	Clean Marine	Polluted Dust
$S_{a,532\ \mathrm{nm}}$ (sr)	40	70	35	70	20	65
$S_{a,1064\ \mathrm{nm}}$ (sr)	55	40	30	30	45	30
Fine fraction by volume	0.223	0.329	0.050	0.531	0.025	0.241
Coarse fraction by volume	0.777	0.671	0.950	0.469	0.975	0.759

2009 all show moderate agreement with the expected S_a for the biomass-burning and smoke models presented by Cattrall et al. and Omar et al. The increase in the aerosol loading beginning on the afternoon of 24 September is evident in the aerosol extinction profiles shown in Figure 4. The back trajectory analysis coupled with the increased fire activity in western Montana and Idaho indicated that this increase in aerosol loading was most likely resulting from advected forest fire smoke. The low S_a associated with biomass-burning aerosols measured from the evening of 24 September through 27 September 2009 show similar trends as with the two models referenced here but are skewed somewhat lower. Measured S_a for biomass-burning aerosols have been shown to be directly related to their age by measuring the corresponding age of the carbon monoxide from the fire emission [*Amiridis et al.*, 2009]. Aged biomass-burning aerosols tend to have higher values for the S_a and lower values for the Ångström coefficient, primarily because of the deposition of the aerosols during the transport [*Amiridis et al.*, 2009]. These observations are consistent with the measurements made over Bozeman, Montana. Fresh or relatively unaged smoke was shown to exhibit even lower S_a, as seen in Figure 3. The relative humidity was also monitored throughout this case study using the MP-DIAL to evaluate the potential for hygroscopic growth of the biomass-burning aerosols. Low moisture content in the boundary layer measured during this case study with the DIAL most likely inhibited the hygroscopic growth of the biomass-burning aerosols.

[22] A plot of the average aerosol volume size distribution retrieved from level 1.5 AERONET aerosol data products is shown in Figure 11 for the duration of this case study. The inset shows the scattering extinction measured at 530 nm using the ground-based integrating nephelometer that was used to extend the lidar aerosol extinction profiles to near the surface. A relatively low aerosol extinction measured at the ground from 21 to 24 September 2009 agrees well with the low AODs measured in Figure 2 during the same time period. The background aerosols present during this time period had a volume size distribution with a weak accumulation mode that supports the low observed Ångström coefficients shown in Figure 7. The increase in the fine-mode fraction of the volume size distribution from 24 to 27 September 2009 corresponded to the inflow of biomass-burning aerosols over the observation site consisting of primarily small particles. The corresponding nephelometer measurements at the ground also reveal an increase in the scattering component of the extinction over the same time period corresponding to the smoke events. The relatively aged biomass burning aerosols were flushed out on the evening of 26 September with downslope easterly winds, which were replaced by two relatively fresh smoke events from fires in western Montana, as seen from Figures 1 and 4b. The volume aerosol size distribution measured on the evening of 26 September indicates that the easterly winds partially flushed out the aerosol coarse mode, resulting in a sporadic increase of the lidar ratio seen in Figure 3b. The accumulation mode during this time was mostly unchanged . A drastic increase in the coarse-mode fraction measured early on 27 September is consistent with the intrusion of the fresh biomass-burning aerosols from the previous evening. The large coarse-mode fraction is attributed to the insufficient time for significant gravitational sedimentation of the larger particles, resulting in lower lidar ratios, as seen in Figure 3 on 27 September. The fine and coarse mode volume fractions for each day are given in Table 3.

[23] The Ångström coefficient, a measure of the spectral dependence of the aerosol extinction, provides an estimate of the average aerosol size distribution. Distributions with an abundance of large particles (like dust) have an Ångström exponent that tends toward zero, while distributions dominated by small particles (like smoke) have a larger Ångström exponent that tends toward 2 [*Eck et al.*, 1999]. The lidar ratio, dependent on both the particle scattering phase function and SSA, is thus dependent on the aerosol size distribution (via $P(180°)$), but also depends on the particle shape and both the real and imaginary refractive indexes. The influences of these multiple dependencies can be seen in Figure 12, which is a scatterplot of the lidar ratios retrieved using the single-channel 532 nm lidar as a function of the Ångström exponent derived from the lidar extinction profile and AOD retrievals at 532 and 830 nm. A mixture of Gaussian grouping techniques was used to describe the general daily trends. The data taken on 23–24 September 2009 were grouped together with a high $S_{a,532}$ value and an Ångström coefficient of less than 1. The data collected on 25 September maintained the larger $S_{a,532}$ values, but the Ångström coefficient increased to approximately 1.5, indicating the presence of smaller aerosol particles consistent with biomass-burning aerosols. The data collected on 26 September 2009 exhibited a notably lower $\mathrm{S}_{\mathrm{a},532}$ value and a still higher Ångström coefficient, as described previously.

Table 2. Aerosol Model Parameters Derived by *Cattrall et al.* [2005]

Optical Physical Property	Biomass Burning	SE Asia	Urban-Industrial	Oceanic	Dust	Rural Continental
$S_{a,550\ \mathrm{nm}}$ (sr)	60 ± 8	58 ± 11	71 ± 10	28 ± 5	42 ± 4	49 ± 8
$S_{a,1020\ \mathrm{nm}}$ (sr)	29 ± 4	39 ± 7	37 ± 5	28 ± 5	35 ± 3	31 ± 5

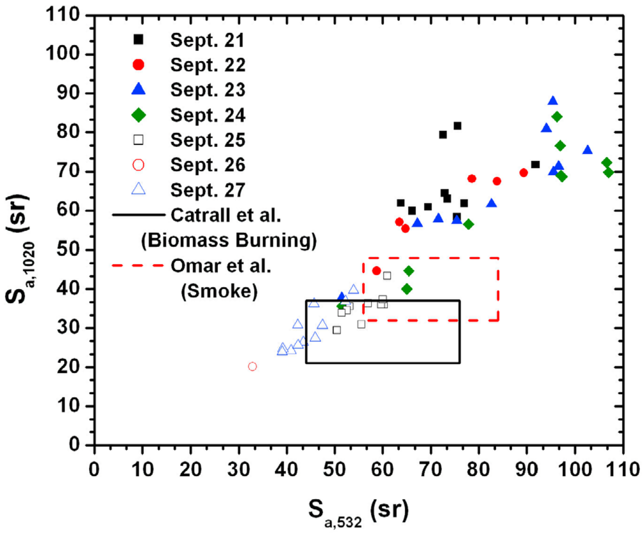

Figure 10. Scatterplot of AERONET S_a retrievals between 532 and 1020 nm over Bozeman, Montana, and the corresponding S_a models for biomass-burning (smoke) aerosol developed by *Cattrall et al.* [2005] and *Omar et al.* [2005].

The data generally cluster into three main groups, the data collected during 23–24 September 2009, the data collected on 25 September 2009, and the data collected on 26 September 2009.

[24] The clustering analysis of the lidar ratio and Ångström coefficient shown in Figure 12 indicates that the aerosols earlier in the week group together and are characterized by high lidar ratios at both 532 and 830 nm, an Ångström coefficient of approximately 1, and a lower fine-mode volume fraction. A transition between the background-polluted continental or highly aged biomass-burning aerosols and the intrusion of the fresher biomass-burning aerosols can be seen on 24 September 2009 as the Ångström coefficient approaches higher values and the S_a begins to decrease. On 25 September 2009, aerosol optical properties were obtained that include higher lidar ratios at both 532and 830 nm, a higher Ångström coefficient, approaching 1.6, and a fine-mode volume fraction consistent with the smoke aerosol model. The two separate clusters seen in Figure 12 for 26 September 2009 are indicative of the flushing out of the aged biomass-burning aerosols and the intrusion of the fresh smoke from nearby forest fire activity. The clusters for this day have significantly lower S_a and higher Ångström coefficients (approaching 2). These results indicate that smaller aerosol particles were present over Bozeman, Montana, on 26 September 2009, consistent with the size distribution retrievals of Figure 11, and that the particles were apparently much less absorptive, as indicated by the lower S_a (Figure 3) and higher SSAs (Figure 5) on that day. Back trajectory analysis for the air mass over Bozeman, Montana, for the same day indicated that the source was most likely from a forest fire burning less than 200 km to the northwest, leaving very little time for the organic changes in these forest fire aerosols to occur before reaching Bozeman.

5. Radiative Forcing

[25] A majority of the negative shortwave direct radiative forcing on the Earth is located between 20°N and 60°N, and

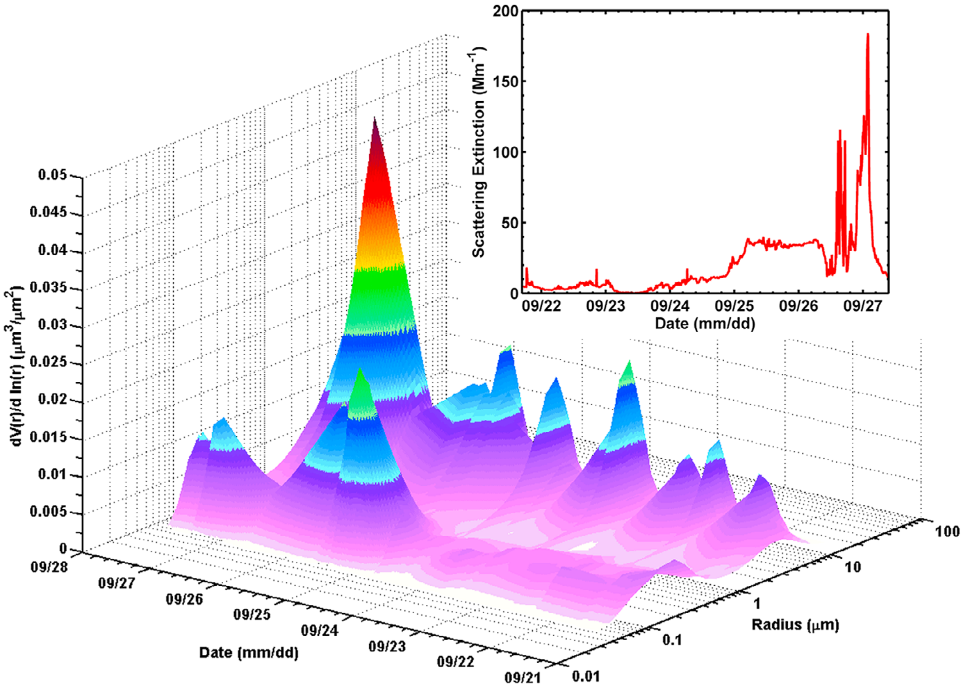

Figure 11. Time series of the aerosol volume size distribution resulting from the AEROENT almucantar scan inversions over Bozeman, Montana. The inset is the scattering component of the aerosol extinction measured at the ground over the same time period using an integrating nephelometer, which was used to extend the lidar extinction profiles to the surface.

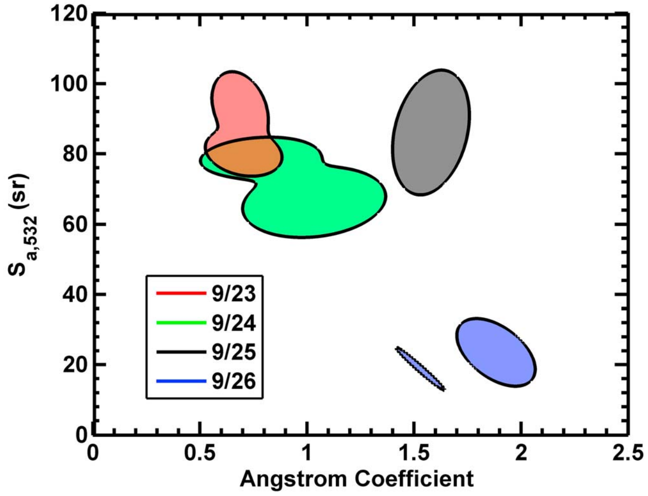

Figure 12. A scatterplot utilizing a mixture of Gaussian grouping techniques of the lidar-retrieved S_a at 532 nm as a function of the lidar-derived Ångström coefficient.

the largest forcing differences between major climate models are at northern midlatitudes such as the observation site in Bozeman, Montana [*Schulz et al.*, 2006]. Remote rural sites such as the one described in this case study show great utility for measuring the direct shortwave radiative effects of anthropogenic aerosol sources over a pristine (i.e., low-AOD) background atmosphere. To begin measuring the effects of biomass-burning aerosols over extremely low background AODs ranging from 0.02 to 0.05 over Bozeman, Montana, a generalized approach to calculating the shortwave direct aerosol radiative forcing was conducted using an AERONET Sun photometer, MODIS, and lidar data. The aerosol direct effect results from the direct interaction of the incoming solar radiation with the aerosols through scattering and absorption [*Shine and Forster*, 1999; *Haywood and Boucher*, 2000; *Yu et al.*, 2006; *Forster et al.*, 2007] resulting in a change of the planetary albedo. The change in the planetary albedo, ΔR_p, resulting from a thin lofted aerosol layer contained within the planetary boundary layer is [*Wendisch et al.*, 2001]

$$\Delta R_p = \frac{\varsigma}{\cos\theta_z}\left[\omega\beta(\theta_z)(1-R_s)^2 - 2R_s(1-\omega)\right], \tag{1}$$

where δ is the aerosol optical depth, θ_z is the solar zenith angle, ω is the single-scatter albedo, $\beta(\theta_z)$ is the backscatter fraction and is a function of the solar zenith angle, and R_s is the surface albedo. The first and second terms in the parentheses on the right-hand side of equation (1) result from the scattering and absorption of the incoming solar radiation by the aerosols, respectively. The backscatter fraction can then be written as [*Wiscombe and Grams*, 1976; *Wendisch et al.*, 2001]

$$\beta(\theta_z) = \frac{1}{2\pi}\int_{(\pi/2)-\theta_z}^{(\pi/2)+\theta_z} P(\theta)[\cot(\theta_z)\cot(\theta)]\sin(\theta)d\theta + \frac{1}{2}\int_{(\pi/2)+\theta_z}^{\pi} P(\theta)\sin(\theta)d\theta, \tag{2}$$

where $P(\theta)$ is the scattering phase function (i.e., as presented in Figure 6). Using a combination of AERONET level 1.5 aerosol data products (SSA, scattering phase function, and AOD) as well as the surface albedo retrieved from the MODIS-Terra MOD04 aerosol data product, the change in the planetary albedo is plotted as a function of time in Figure 13. The sensitivity of the planetary albedo during the morning and evening hours results from the increased backscatter fraction associated with larger solar zenith angles [*Wendisch et al.*, 2001].

[26] The TOA radiative forcing resulting from the aerosol direct effect can then be written in terms of the change in the planetary albedo and the solar zenith angle. The direct shortwave radiative forcing is expressed as [*Wendisch et al.*, 2001]

$$F = -\int \cos(\theta_z)S_o(\lambda)T^2(1-A_c)\Delta R_p(\lambda)d\lambda, \tag{3}$$

where $S_0(\lambda)$ is the solar constant per unit wavelength at the TOA, T is the transmission from the TOA to the top of the planetary boundary layer, and A_c is the fractional cloud cover, which was assumed to be zero during the majority of this case study. The solar constant per unit wavelength was calculated by modeling the Sun as a blackbody radiator with a surface temperature of 5800 K. The solar constant per unit wavelength was normalized so the integration of $S_0(\lambda)$ as a function of wavelength yields a total solar constant of 1370 W/m^2. The change in the planetary albedo (equation (1)) over the whole solar spectrum was calculated at the discrete MODIS and AEROENT direct and sky scan spectral bands. This method makes the assumption that the planetary albedo is constant over the wavelength range separating any two successive channels and also that the solar irradiances below and above 440 and 1020 nm, respectively, are negligible and assumed to be equal to the values at those two channels. The total shortwave direct radiative forcing as a function of time is shown in Figure 14. Similar to the diurnal trends seen in the planetary albedo shown in Figure 13, the diurnal changes in the radiative forcing occurring each day also resulted from the increasing backscatter fraction for the larger solar zenith angles in the morning and evening. Between 21 and 24 September 2009, the radiative forcing resulting from the aerosol direct effect increased because of the decreasing

Table 3. Average Daily AERONET Fine- and Coarse-Mode Volume Fractions

	21 Sep	22 Sep	23 Sep	24 Sep	25 Sep	26 Sep	27 Sep
Fine-mode volume fraction	0.5166	0.4133	0.3552	0.3984	0.5185	0.4050	0.2845
Coarse-mode volume fraction	0.4834	0.5867	0.6448	0.6016	0.4815	0.5950	0.7155

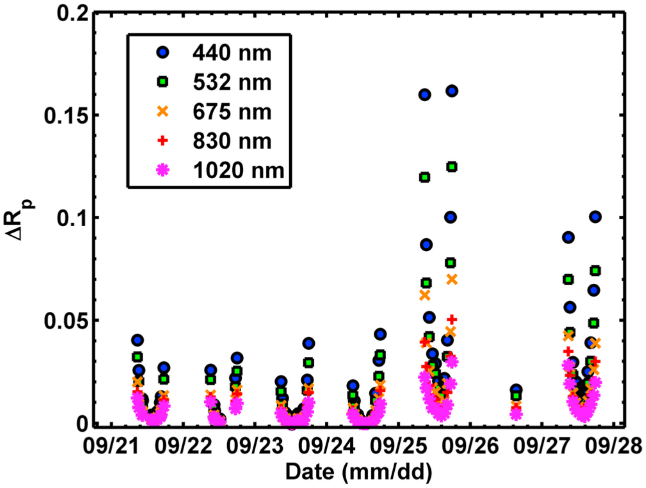

Figure 13. Time series of the change in the planetary albedo resulting from the aerosol direct effect calculated using MODIS-Terra MOD04 surface albedo measurements and AERONET aerosol optical properties.

SSA seen in Figure 5, which corresponds to increased absorption. The decrease in the radiative forcing seen during 25–27 September 2009 correlates with the increased aerosol loading that was due to the forest fires burning in western Montana and Idaho.

[27] The ability to monitor aerosol optical properties using ground-based instruments provides detailed temporal information that can be used to estimate the radiative forcing of the aerosol direct effect at a single location. Using combined regional MODIS (AOD, surface albedo) data and AERONET (SSA, scattering phase function) data retrieved over Bozeman, Montana, an estimate of the radiative forcing over the northwestern United States for 24–27 September 2009 was calculated based on equations (1)–(3) presented earlier in this section. The results of these calculations are shown in Figure 15. The shortwave direct radiative forcing resulting from the aerosol direct effect calculated using the MODIS-retrieved AOD and the SSA and scattering phase function from AERONET compared favorably with the radiative forcing calculated using the AOD from AERONET, as seen in Figure 14. Large net negative radiative forcings can be seen in which high AODs dominated as a result of biomass-burning aerosols from Figure 1. The broad aged smoke plume transported from the northwest on 25 September as well as the directed fresh smoke from western Montana on 27 September can be seen to result in relatively large net negative radiative forcings over Bozeman, Montana. The satellite- and ground-based active and passive remote sensors used to calculate the shortwave direct radiative forcing over Bozeman, Montana, show reasonable agreement with one another. Large errors can arise when attempting to estimate regional shortwave direct radiative forcing effects as a result of atmospheric aerosol loading using data from a single geographical location coupled with large-swath satellite data, such as the case study presented here. Although reasonable agreement between the direct aerosol radiative forcing effect calculated using ground-based and satellite-based remote sensors was seen over Bozeman, Montana, care must be taken in estimating the regional aerosol direct forcing over larger geographical regions. A validation study using the WRF chemical transport model, numerous AERONET sites, as well as the same suite of instruments described in this case study has begun to investigate the accuracy of calculating the aerosol direct effect over larger geographical regions using aerosol optical properties retrieved from a single location.

6. Conclusions

[28] Aerosol optical properties were observed over Bozeman, Montana, from 21 to 27 September 2009 during a period transitioning from an initial low-AOD background atmosphere consisting primarily of a combination of very well aged biomass-burning aerosols and polluted continental aerosols with AODs of less than 0.05 at 532 nm at the beginning of the observational period to a maximum aerosol optical depth of 0.17 at 532 nm resulting from advected biomass-burning aerosol from forest fires burning in the northwestern United States. The aerosol optical properties monitored during this observational period were combined and compared with aerosol models developed by *Cattrall et al.* [2005] and *Omar et al.* [2005] as well as with back trajectory analyses to study the differences and similarities in optical properties during intervals in which background, aged smoke, or fresh smoke dominated the AOD. Diurnal fluctuations in the S_a of the weakly present background aged smoke or continental aerosols during the first half of the observational period derived from the two lidars ranged between 55 and 95 sr (50 and 95 sr) at 532 nm (830 nm) and showed good agreement with AERONET measurements as well as with Mie scattering computations. Although in agreement with two other partially independent determinations of S_a, the S_a were still consistently higher than predicted by aerosol models for polluted continental-urban or biomass-burning aerosols. This is thought to be primarily a result of a mixture of polluted continental aerosols and highly aged and absorptive smoke with a weak accumulation mode in the aerosol volume size distribution. S_a retrieved in the latter

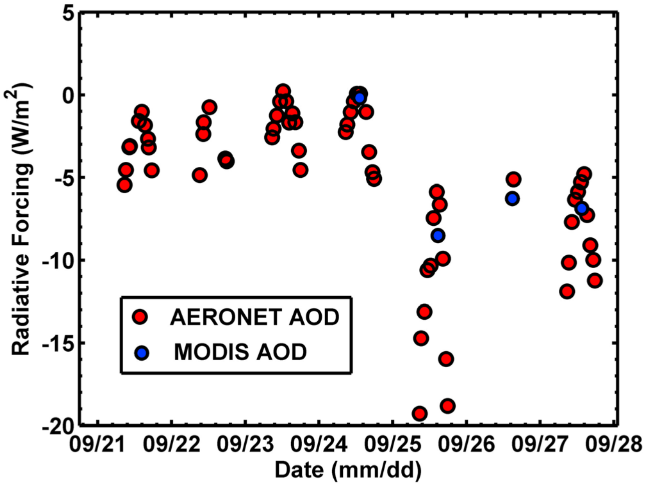

Figure 14. Time series comparing the estimated total shortwave radiative forcing resulting from the aerosol direct effect for AOD measurements obtained from AERONET and MODIS-Terra.

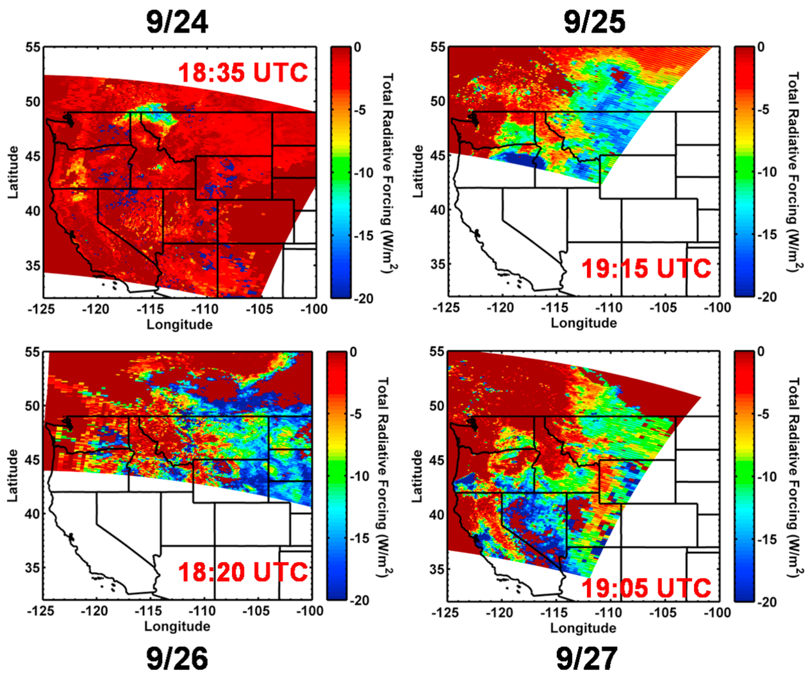

Figure 15. Estimation of the shortwave direct radiative forcing (W/m^2) over the northwestern United States using MODIS–Terra AOD/surface albedo measurements and AERONET-derived aerosol optical properties measured over Bozeman, Montana.

half of the observational period for the aged but yet relatively fresh biomass-burning aerosol ranged between 60 and 80 sr (50 and 70 sr) at 532 nm (830 nm) and were fairly consistent with the aerosol model predictions, although the very fresh biomass-burning aerosols from western Montana were shown to exhibit very low S_a. These low-S_a retrievals from both the lidar and the CIMEL solar radiometer observations showed good agreement, but were consistently lower than the referenced biomass-burning aerosol models, which was most likely a result of insufficient time for gravitational sedimentation of the large aerosol as well as the aging process to occur.

[29] The shortwave radiative forcing resulting from the aerosol direct effect was estimated using a combination of both ground-based and satellite data. The diurnal cycle of the radiative forcing resulted from the changing backscatter fraction that was due to the phase function and the time-varying solar zenith angle. A daily average shortwave direct radiative forcing of approximately −2 W/m^2 was observed for a low-AOD background atmosphere consisting primarily of a combination of well-aged biomass-burning aerosols and polluted continental aerosols during the beginning half of the case study. A net negative cooling associated with the influx of biomass-burning aerosols during the second half of the case study yielded an average radiative forcing of approximately −10 W/m^2. Reasonable agreement between the shortwave direct radiative forcing calculated using a combination of ground- and satellite-based data and the radiative forcing calculated using primarily the satellite data was seen over the duration of this case study. Validation to investigate the accuracy of calculating the aerosol direct effect over larger geographical regions using aerosol optical properties retrieved from a single location is underway by coupling inputs from the WRF chemical transport model, lidar data, and AERONET data from regional sites. These types of studies can help in a better understanding of the role of atmospheric aerosols on the radiative forcing of the climate system and provide information for inclusion of representative aerosol models for climate modeling. This work represents initial steps by researchers at Montana State University to develop a set of complimentary remote sensing tools for long-term aerosol studies from a clean continental site.

[30] **Acknowledgments.** This work was supported by NASA EPSCoR under grant NNX08AT69A and the NASA Graduate Student Researchers Program (GSRP) under grant NNX08AR90H. The authors would like to thank Kevin Repasky and Joe Shaw and their staff for establishing and maintaining the Bozeman, Montana, AERONET site used in this investigation. The authors would also like to thank Joe Shaw for the use of the scattering nephelometer and weather station data used in this case study.

References

Amiridis, V., D. S. Balis, E. Giannakaki, A. Stohl, S. Kazadzis, M. E. Koukouli, and P. Zanis (2009), Optical characteristics of biomass burning aerosols over southeastern Europe determined from UV-Raman lidar measurements, *Atmos. Chem. Phys.*, *9*, 2431–2440, doi:10.5194/acp-9-2431-2009.

Burton, S. P., et al. (2010), Using airborne high spectral resolution lidar data to evaluate combined active plus passive retrievals of aerosol extinction profiles, *J. Geophys. Res.*, *115*, D00H15, doi:10.1029/2009JD012130.

Cattrall, C., J. Reagan, K. Thome, and O. Dubovik (2005), Variability of aerosol and spectral lidar and backscatter and extinction ratios for key aerosol types derived from selected Aerosol Robotic Network locations, *J. Geophys. Res.*, *110*, D10S11, doi:10.1029/2004JD005124.

Charlson, R. J., J. Langner, H. Rodhe, C. B. Leovy, and S. G. Warren (1991), Perturbation of the northern hemisphere radiative balance by backscattering from anthropogenic sulfate aerosols, *Tellus, Ser. A*, *43*, 152–163, doi:10.1034/j.1600-0870.1991.00013.x.

Charlson, R. J., S. E. Schwartz, J. M. Hales, R. D. Cess, J. A. Coakley, J. E. Hansen, and D. F. Hoffman (1992), Climate forcing by anthropogenic aerosols, *Science*, *255*, 423–430, doi:10.1126/science.255.5043.423.

Chylek, P., and J. Wong (1995), Effects of absorbing aerosols on global radiation budget, *Geophys. Res. Lett.*, *22*(8), 929–931, doi:10.1029/95GL00800.

Coakley, J. A., and P. Chylek (1975), The two-stream approximation in radiative transfer: Including the angle of the incident radiation, *J. Atmos. Sci.*, *32*, 409–418, doi:10.1175/1520-0469(1975)032<0409:TTSAIR>2.0.CO;2.

Dubovik, O., and M. D. King (2000), A flexible inversion algorithm for retrieval of aerosol optical properties from Sun and sky radiance measurements, *J. Geophys. Res.*, *105*(D16), 20,673–20,696, doi:10.1029/2000JD900282.

Dubovik, O., A. Smirnov, B. N. Holben, M. D. King, Y. J. Kaufman, T. F. Eck, and I. Slutsker (2000), Accuracy assessments of aerosol optical properties retrieved from Aerosol Robotic Network (AERONET) Sun and sky radiance measurements, *J. Geophys. Res.*, *105*(D8), 9791–9806, doi:10.1029/2000JD900040.

Eck, T. F., B. N. Holben, J. S. Reid, O. Dubovik, A. Smirnov, N. T. O'Neill, I. Slutsker, and S. Kinne (1999), Wavelength dependence of the aerosol optical depth of biomass burning, urban, and desert dust aerosols, *J. Geophys. Res.*, *104*(D24), 31,333–31,349, doi:10.1029/1999JD900923.

Fernald, F. G. (1984), Analysis of atmospheric lidar applications: Some comments, *Appl. Opt.*, *23*, 652–653, doi:10.1364/AO.23.000652.

Fernald, F. G., B. M. Herman, and J. A. Reagan (1972), Determination of aerosol height distributions by lidar, *J. Appl. Meteorol.*, *11*, 482–489, doi:10.1175/1520-0450(1972)011<0482:DOAHDB>2.0.CO;2.

Ferrare, R., G. Feingold, S. Ghan, J. Ogren, B. Schmid, S. E. Schwartz, and P. Sheridan (2006), Preface to special section: Atmospheric Radiation Measurement Program May 2003 Intensive Operation Period examining aerosol properties and radiative influences, *J. Geophys. Res.*, *111*, D05S01, doi:10.1029/2005JD006908.

Forster, P., et al. (2007), Changes in atmospheric constituents and in radiative forcing, in *Climate Change 2007: The Physical Science Basis, Contributions of Working Group I to the Fourth Assessment Report of the Intergovernmental Panel on Climate Change*, edited by S. Solomon et al., Cambridge Univ. Press, Cambridge, U. K.

Hallar, A. G., et al. (2006), Atmospheric Radiation Measurements Aerosol Intensive Operating Period: Comparison of aerosol scattering during coordinated flights, *J. Geophys. Res.*, *111*, D05S09, doi:10.1029/2005JD006250.

Haywood, J., and O. Boucher (2000), Estimates of the direct and indirect radiative forcing due to tropospheric aerosols: A review, *Rev. Geophys.*, *38*(4), 513–543, doi:10.1029/1999RG000078.

Haywood, J. M., and K. P. Shine (1995), The effect of anthropogenic sulfate and soot aerosol on the clear sky planetary radiation budget, *Geophys. Res. Lett.*, *22*(5), 603–606, doi:10.1029/95GL00075.

Holben, B. N., et al. (1998), AERONET—A federated instrument network and data archive for aerosol characterization, *Remote Sens. Environ.*, *66*(1), 1–16, doi:10.1016/S0034-4257(98)00031-5.

Holben, B. N., et al. (2001), An emerging ground-based aerosol climatology: Aerosol optical depth from AERONET, *J. Geophys. Res.*, *106*(D11), 12,067–12,097, doi:10.1029/2001JD900014.

Johnson, B. T., S. Christopher, J. M. Haywood, S. R. Osborne, S. McFarlane, C. Hsu, C. Salustro, and R. Kahn (2009), Measurement of aerosol optical properties from aircraft, satellite, and ground-based remote sensing: A case-study from the dust and biomass-burning experiment (DABEX), *Q. J. Meteorol. Soc.*, *135*, 922–934, doi:10.1002/qj.420.

Kovalev, V. A., and W. E. Eichinger (2004), *Elastic Lidar, Theory, Practice, and Analysis Methods*, John Wiley, Hoboken, N. J., doi:10.1002/0471643173.

Loeb, N. G., and N. Manalo-Smith (2005), Top-of-atmosphere direct radiative effect of aerosols over global oceans from merged CERES and MODIS observations, *J. Clim.*, *18*, 3506–3526, doi:10.1175/JCLI3504.1.

McComiskey, A., S. E. Schwartz, B. Schmid, H. Guan, E. R. Lewis, P. Ricchiazzi, and J. A. Ogren (2008), Direct aerosol forcing: Calculation from observables and sensitivities to inputs, *J. Geophys. Res.*, *113*, D09202, doi:10.1029/2007JD009170.

McPherson, C. J., J. A. Reagan, J. Schafer, D. Giles, R. Ferrare, J. Hair, and C. Hostetler (2010), AERONET, airborne HSRL, and CALIPSO aerosol retrievals compared and combined: A case study, *J. Geophys. Res.*, *115*, D00H21, doi:10.1029/2009JD012389.

Moffet, R. C., and K. A. Prather (2009), In-situ measurements of mixing state and optical properties of soot with implications for raditive forcing estimates, *Proc. Natl. Acad. Sci. U. S. A.*, *106*(29), 11,872–11,877, doi:10.1073/pnas.0900040106.

Moosmüller, H., and W. P. Arnott (2003), Angular truncation errors in integrating nephelometry, *Rev. Sci. Instrum.*, *74*(7), 3492–3501, doi:10.1063/1.1581355.

Nehrir, A. R., K. S. Repasky, and J. L. Carlsten (2011), Eye-safe diode-laser-based micropulse differential absorption lidar (DIAL) for water vapor profiling in the lower troposphere, *J. Atmos. Oceanic Technol.*, *28*, 131–147, doi:10.1175/2010JTECHA1452.1.

Nehrir, A. R., K. S. Repasky, J. L. Carlsten, M. D. Obland, and J. A. Shaw (2009), Water vapor profiling using a widely tunable, amplified diode laser based differential absorption lLidar (DIAL), *J. Atmos. Oceanic Technol.*, *26*, 733–745, doi:10.1175/2008JTECHA1201.1.

Nemesure, S., R. Wagener, and S. E. Schwartz (1995), Direct shortwave forcing of climate by the anthropogenic sulfate aerosol: Sensitivity to particle size, composition, and relative humidity, *J. Geophys. Res.*, *100*(D12), 26,105–26,116, doi:10.1029/95JD02897.

Omar, A. H., J. Won, D. M. Winker, S. Yoon, O. Dubovik, and M. P. McCormick (2005), Development of global aerosol models using cluster analysis of Aerosol Robotic Network (AERONET) measurements, *J. Geophys. Res.*, *110*, D10S14, doi:10.1029/2004JD004874.

Omar, A. H., et al. (2009), The CALIPSO Automated Aerosol Classification and Lidar Ratio Selection Algorithm, *J. Atmos. Oceanic Technol.*, *26*, 1994–2014, doi:10.1175/2009JTECHA1231.1.

Pahlow, M., D. Muller, M. Tesche, H. Eichler, G. Feingold, W. L. Eberhand, and Y.-F. Cheng (2006), Retrieval of aerosol properties from combined multiwavelength lidar and sunphotometer measurements, *Appl. Opt.*, *45*(28), 7429–7442, doi:10.1364/AO.45.007429.

Reagan, J. A., X. Wang, C. Cattrall, and K. Thome (2004), Spaceborne lidar aerosol retrieval approaches based on aerosol model constraints, in *2004 IEEE International Geoscience and Remote Sensing Symposium, 2004. IGARSS '04. Proceedings*, vol. 3, pp. 1940–1943, IEEE, New York, doi:10.1109/IGARSS.2004.1370723.

Reagan, J. A., X. Wang, S. Palm, and J. Spinhirne (2006), Lidar aerosol retrievals from Icesat using a model based constrained ratio approach, paper presented at the 12th Conference on Atmospheric Radiation, Am. Meteorol. Soc., Madison, Wisc., 10–14 July.

Reagan, J. A., C. J. McPherson, C. A. Hostetler, J. W. Hair, and R. A. Ferrare (2007), Initial CRAM aerosol retrievals from CALIPSO and supporting airborne HSRL measurements, *IEEE International Geoscience and Remote Sensing Symposium, 2007. IGARSS 2007*, pp. 4979–4982, IEEE, New York.

Repasky, K. S., J. A. Reagan, A. R. Nehrir, D. S. Hoffman, M. J. Thomas, J. L. Carlsten, J. A. Shaw, and G. E. Shaw (2011), Observational studies of atmospheric aerosols over Bozeman, Montana using a two color lidar, a water vapor DIAL, a solar radiometer, and a ground based nephelometer over a twenty four hour period, *J. Atmos. Oceanic Technol.*, *28*, 320–336, doi:10.1175/2010JTECHA1463.1.

Ricchiazzi, P., C. Gautier, J. A. Ogren, and B. Schmid (2006), A comparison of optical properties obtained from in situ measurements and retrieved Sun and sky radiaince observations during the May 2003 ARM Aerosol Intensive Observation Period, *J. Geophys. Res.*, *111*, D05S06, doi:10.1029/2005JD005863.

Russell, P. B., J. M. Livingston, and E. E. Uthe (1979), Aerosol induced albedo change: Measurement and modeling of an incident, *J. Atmos. Sci.*, *36*, 1587–1608, doi:10.1175/1520-0469(1979)036<1587:AIACMA>2.0.CO;2.

Russell, P. B., S. A. Kinne, and R. W. Bergstrom (1997), Aerosol climate effects: Local radiative forcing and column closure experiments, *J. Geophys. Res.*, *102*(D8), 9397–9407, doi:10.1029/97JD00112.

Schulz, M., et al. (2006), Radiative forcing by aerosols as derived from the AeroCom present-day and pre-industrial simulations, *Atmos. Chem. Phys.*, *6*, 5225–5246, doi:10.5194/acp-6-5225-2006.

Shine, K. P. and P. M. de F. Forster (1999), The effect of human activity on radiative forcing of climate change: A review of recent development, *Global Planet. Change*, *20*, 205–225, doi:10.1016/S0921-8181(99)00017-X.

Smirnov, A., B. N. Holben, T. F. Eck, O. Dubovik, and I. Slutsker (2000), Cloud-screening and quality control algorithms for the AERONET database, *Remote Sens. Environ.*, *73*, 337–349, doi:10.1016/S0034-4257(00)00109-7.

Wendisch, M., J. Heintzenberg, and M. Bussemer (2001), Measurement-based aerosol forcing calculations: The influence of model complexity, *Meteorol. Z.*, *10*(1), 45–60, doi:10.1127/0941-2948/2001/0010-0045.

Wiscombe, W. J., and G. W. Grams (1976), The backscatter fraction in the two-stream approximation, *J. Atmos. Sci.*, *33*, 2440–2451, doi:10.1175/1520-0469(1976)033<2440:TBFITS>2.0.CO;2.

Yu, H. Y., et al. (2006), A review of measurement-based assessments of the aerosol direct radiative effect and forcing, *Atmos. Chem. Phys.*, *6*, 613–666, doi:10.5194/acp-6-613-2006.

J. L. Carlsten, Physics Department, 264 EPS, Montana State University, Bozeman, MT 59717, USA.

A. R. Nehrir and K. S. Repasky, Department of Electrical and Computer Engineering, Cobleigh Hall Room 610, Montana State University, Bozeman, MT 59717, USA. (arnehrir@gmail.com)

J. A. Reagan, Department of Electrical and Computer Engineering, University of Arizona, 1230 E. Speedway, Bldg. 104, Tucson, AZ 85721, USA.